
Pathology Steered Stratification Network for Subtype Identification in Alzheimer's Disease

Enze Xu^{1, #}, Jingwen Zhang^{1, #}, Jiadi Li², Defu Yang³, Guorong Wu^{3,4}, and Minghan Chen^{1,*}

¹Department of Computer Science, Wake Forest University, Winston-Salem, NC, USA

²Department of Psychology, Wake Forest University, Winston-Salem, NC, USA

³Department of Psychiatry, University of North Carolina at Chapel Hill, Chapel Hill, NC, USA

⁴Department of Computer Science, University of North Carolina at Chapel Hill, Chapel Hill, NC, USA

#Equal contribution *To whom correspondence should be addressed.

Abstract

Motivation: Alzheimer's disease (AD) is a heterogeneous, multifactorial neurodegenerative disorder characterized by three neurobiological factors beta-amyloid, pathologic tau, and neurodegeneration. The massive heterogeneity between neurobiological examinations and clinical assessment is the current biggest challenge in the early diagnosis of Alzheimer's disease, urging for a comprehensive stratification of the aging population that is defined by reliable neurobiological biomarkers and closely associated with clinical outcomes. However, existing statistical inference approaches in neuroimaging studies of AD subtype identification fail to take into account the neuropathological domain knowledge, which could lead to ill-posed results that are sometimes inconsistent with the essential neurological principles.

Results: To fill this knowledge gap, we propose a novel pathology steered stratification network (PSSN) that integrates mainstream AD pathology with multimodal longitudinal neuroimaging data to categorize the aging population. By combining theory-based biological modeling and data-driven deep learning, this cross-disciplinary approach can not only generate long-term biomarker prediction consistent with the end-state of individuals, but also stratifies subjects into fine-grained subtypes with distinct neurological underpinnings across subtypes, while aging brains within the same subtype share common biological behaviors that emerge as similar trajectories of cognitive decline. Our stratification outperforms K-means and SuStain in both inter-cluster heterogeneity and intra-cluster homogeneity of various clinical scores. Importantly, we identify six subtypes spanning AD spectrum, where each subtype exhibits a distinctive biomarker pattern that is consistent with its clinical outcome. A disease evolutionary graph is further provided by quantifying subtype transition probabilities, which may assist pre-symptomatic diagnosis and guide therapeutic treatments.

Contact: chenm@wfu.edu

1 Introduction

Alzheimer's disease (AD), one of the common neurodegenerative disorders, causes progressive memory loss, cognitive decline, behavioral disturbance, functional dependence, and ultimately death (Braak and Braak 1991). No effective treatments for AD have been found so far, urging the need for early diagnosis and intervention. Current diagnostic systems for AD primarily rely upon clinical signs and symptoms. However, neuropsychological assessments alone are inadequate to reflect the underlying pathophysiological progressions considering the long preclinical period and diverse symptoms across individuals (Dickerson et al. 2007; Aisen et al. 2010; Braak and Braak 1996). Additionally, post-mortem histological examination of AD pathology in brain tissue samples often does not align closely with clinical diagnosis (Ikonomovic et al. 2016). This body of evidence further underscores the significant gap between symptomatic manifestations and latent development of AD pathology (Clifford R. Jack Jr et al. 2009; Cope et al. 2018; Holtzman, Morris, and Goate 2011). Therefore, to facilitate accurate prognosis and prompt intervention of AD, it is critical to stratify the aging population into fine-grained subtypes that are not only closely correlated with clinical outcomes but also characterize biomarker progression of cognitive decline.

According to the 2018 NIA-AA (National Institute on Aging and Alzheimer's Association) research framework (Clifford R. Jack et al. 2018), accumulations of beta-amyloid plaques (A) and pathologic tau (T), along with neurodegeneration ([N]), are considered the three pathological hallmarks of Alzheimer's disease progression. With recent advancement and accessibility of neuroimaging techniques, spatial data for biomarkers and atrophy patterns becomes increasingly available for clinical and research purposes. Striking efforts have been made to understand and explain the heterogeneity in AD progression from neuroimaging data (Li, Yang, et al. 2022; Habes et al. 2020; Lam et al. 2013), among which statistical inference, mostly machine learning approaches, have proven its promising potential in AD subtype identification (Ding et al. 2019; Aksman et al. 2021; Venugopalan et al. 2021). For example, a Subtype and Stage Inference (SuStIn) was developed to predict temporal patterns and identify AD subtypes from cross-sectional magnetic resonance imaging (MRI) progression patterns (Young et al. 2018). Vogel et al. extended the SuStIn to include tau biomarker and identified four distinct progression subtypes (Vogel et al. 2021). Recently, a semi-supervised clustering via generative adversarial networks (Smile-GAN) was proposed to cluster subjects with distinct progression pathways using brain atrophy measurements (Yang et al. 2021). However, those methods including most existing machine learning analyses fail to take into account the underlying pathological mechanism of AD, which may result in ill-posed results that are inconsistent with essential biological laws.

Different from statistical inference approaches, mathematical modeling predicts disease progression based on existing knowledge of AD pathology (Bertsch et al. 2021). Several models have been proposed to simulate the propagation pattern of biomarkers. For example, an ordinary differential equation (ODE) system was constructed to mathematically model the temporal progression of amyloid and neuronal dysfunction (Bertsch et al. 2017). Following the diffusive nature of amyloid and tau, network diffusion models were developed to predict longitudinal patterns of atrophy and metabolism in AD across brain networks (Raj, Kuceyeski, and Weiner 2012; Raj et al. 2015). This pioneering work has shown the potential of capturing macroscopic properties of disease progression from a systems biology perspective. Hao et.al proposed a PDE-based (partial differential equation) system biology model to investigate the complex molecular pathways underlying AD (Hao and Friedman 2016). But this model was

not designed on real brain domain and was restricted to theoretical analysis due to the lack of real data validation. Recently, a network guided reaction-diffusion model was proposed to integrate both the interactions between AT[N] biomarkers and the diffusions along structural brain networks, which encodes the prevailing pathological mechanisms of AD and captures biomarker dynamics of individuals (J. Zhang et al. 2020). While those studies demonstrated the role of neurobiological factors in heterogeneous trajectories of cognitive decline (C.R. Jack et al. 2004; D. K. Johnson et al. 2009; Raj 2021), a comprehensive analysis of phenotypic heterogeneity is still lacking, which limits their applicability to general population.

To disentangle the heterogenous neurodegeneration trajectories, we propose a novel pathology steered stratification network (PSSN) based on the combined power of data-driven deep learning and theory-based biological modeling. Our approach is integrated with existing neuropathological mechanisms and is evaluated on significant multimodal longitudinal imaging scans covering the full spectrum of cognitive states (from cognitive normal to AD), allowing the model to be trained on different progression paths. To the best of our knowledge, the proposed computational framework is the first subtype identification tool that jointly considers the biomarker pathological interactions, brain network diffusions, and clinical assessments for population stratification. Leveraging theory-based biological models and data-driven deep learning, our PSSN

- incorporates neuropathological domain knowledge to ensure neurologically consistent results;
- ameliorates the limitation of sparse longitudinal imaging data by learning the spatiotemporal dynamics of AT[N] biomarkers;
- stratifies subjects into fine-grained subtypes with distinct neurological underpinnings and phenotypic outcomes;
- characterizes subtype transition path on AD spectrum, providing insight into pre-symptomatic prognosis and prevention.

2 Methods

2.1 Reaction-Diffusion Model

Based on existing neuropathological knowledge, we first construct a reaction-diffusion model of Alzheimer's disease to characterize the spatiotemporal interaction and diffusion of AT[N] biomarkers. This biological model can predict subject-specific long-term propagation patterns across brain networks, which enables PSSN to identify AD subtypes following neurological principles.

Model Entity. Let M denote the number of subjects included in our model. As shown in Fig. 1(a), the model takes four entities of AD as input: (i) amyloid level measured from Amyloid PET; (ii) tau level measured from Tau PET; (iii) neuronal loss measured from FDG-PET; (iv) graph Laplacian calculated from DWI (diffusion-weighted imaging), which is a 148×148 matrix characterizing brain structural topology. Each AT[N] input is a $148 \times M$ matrix, where 148 is the number of brain regions after image parcellation. These multimodal neuroimaging data jointly provide a comprehensive AD profile of each subject.

Model Design. In Fig. 1(b), the core of our reaction-diffusion model is the amyloid cascade hypothesis (Petrella et al. 2019; Clifford R. Jack and Holtzman 2013; Bloom 2014; Busche and Hyman 2020; Ballatore, Lee, and Trojanowski 2007). (i) Amyloid activates hyperphosphorylation of tau, tau triggers subsequent neurodegeneration, and damaged neurons release more amyloid to the brain (dashed arrows) (Frost and Li 2017). (ii) amyloid and tau have constant production (solid arrows) and density-

based degradation (hollow arrows). (iii) neuronal resilience moderates the rate of neurodegeneration (Y. Zhang et al. 2020). (vi) amyloid and tau diffuse along the structural brain network via Laplacian operator (Raj et al. 2015; Li, Zhao, et al. 2022). This model quantitatively characterizes the spatiotemporal dynamics of AT[N] biomarkers (Fig. 1(c)), laying a solid foundation for AD prognostic subtype identification. Detailed descriptions can be found in (J. Zhang et al. 2020).

2.2 Pathology Steered Stratification Network

Following our biological model, we construct a deep predictive neural network to disentangle the heterogenous neurodegeneration progression and stratify subjects into fine-grained subtypes within distinct neurobiological underpinnings.

Data Fusion. Let t_m denote the number of clinical assessments for subject m . For each subject m , we (1) predict the trajectories of AT[N] biomarkers using the reaction-diffusion model; (2) select t_m points from subject m 's trajectory correspond to the time points of clinical assessments, concatenate AT[N] data $\{A_1, \dots, A_{148}, T_1, \dots, T_{148}, N_1, \dots, N_{148}\}$ and the diagonal elements of Laplacian matrix $\{L_1, \dots, L_{148}\}$ for each $t \in \{1, \dots, t_m\}$ to generate a $592 \times t_m$ matrix, which serves as the input to our stratification network; and (3) extract clinical assessments of subject m as output, which includes mini-mental state examination (MMSE), Alzheimer's disease assessment scale (ADAS), and clinical dementia rating (CDR). Thus for a total population of M , we have an input matrix $X = \{X_m^t | m = 1, \dots, M, t = 1, \dots, t_m\}$, where each X_m^t represents the AT[N]-Net data of subject m at visit t , and output matrix $Y = \{Y_m^t | m = 1, \dots, M, t = 1, \dots, t_m\}$, where Y_m^t represents the three clinical scores of subject m at visit t .

Stratification Network. We aim to stratify aging brains into a set of subtypes, written as $S = \{S_m^t | m = 1, \dots, M, t = 1, \dots, t_m\}$, where S_m^t is the subtype index for subject m at the t^{th} visit. To distinct neurobiological underpinnings between subtypes as well as preserve the shared symptoms and cognitive decline patterns within each subtype, three sub-networks are proposed as follows.

Feature Extraction Network (Fig. 1(d)). The feature extraction network is a many-to-many Long Short-Term Memory (LSTM) network to learn representative features of each sample. For each input sample X_m^t of subject m at the t^{th} visit, the corresponding AT[N]-Net data is reduced to a feature vector in a lower-dimensional space, represented as an AT[N]-Net feature vector $P_m^t = P_\theta(X_m^1, X_m^2, \dots, X_m^t)$, P_θ is the feature representation learning network, and θ denotes the parameters of the network.

Subtype Network (Fig. 1(e)). The subtype network is a fully connected neural network that learns patterns in the subject pool and then maps each AT[N]-Net feature vector P_m^t into a subtype-specific feature vector $C_m^t(k)$, where $k \in \{1, 2, \dots, K\}$ and K denotes the number of identified subtypes. Also, we include fuzzy assignment by minimizing the entropy-based regularization term $E_m^t = -\sum_{k=1}^K C_m^t(k) \log(C_m^t(k))$ to avoid the trivial stratification solution (one dominant cluster). Let ψ denote the parameters of subtype network.

Prediction Network (Fig. 1(f)). We use a fully connected neural network to predict each subject's MMSE, CDR and ADAS scores based on the subtype assignment probability C_m^t generated in Subtype Network. A L_2 -norm loss function is used to measure the prediction error, written as $l_m^t = \|Y_m^t - \hat{Y}_m^t\|^2$. This clinical assessment-guided feature allows us to group subjects with similar clinical stages. Let ϕ denote the parameters of the prediction network.

Optimization. Three sub-networks are jointly updated by the loss function

$$L(\theta, \psi, \phi) = \sum_{m=1}^M \sum_{t=1}^{t_m} (l_m^t + \lambda \cdot E_m^t(k)),$$

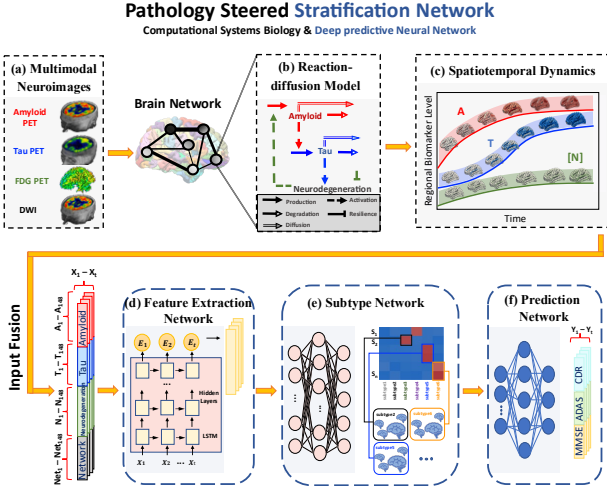


Fig. 1. Pathology Steered Stratification Framework: A novel integration of a systems biology model and deep predictive neural network. (a) Multimodal longitudinal neuroimages input: Amyloid-, Tau-, FDG-PET, and DWI scans are processed to indicate regional amyloid, tau, neurodegeneration, and network connectivity level (AT[N]-Net), respectively. (b) Reaction-diffusion Model: a diffusive AT[N] cascade model was proposed based on several canonical AD pathways. (c) Spatiotemporal Dynamics: reaction-diffusion model generates subject-specific long-term AT[N] trajectory prediction. (d) Feature Extraction Network: an LSTM network learns a lower-dimension representative feature from the predicted trajectories and structural network. (e) Subtype Network: a fully connected neural network that classifies the learned features to the subtype-probability vectors. (f) Prediction Network: a fully connected neural network that predicts clinical assessments using the subtype-probability vectors.

where l_m^t allows clinical assessments to guide the stratification process and λ is a hyperparameter used to control the level of fuzzy assignment. Directly calculating the backpropagation derivative is quite complicated in the Stratification network, as it aims to minimize the divergence between clinical scores and predictions as well as to find the optimal cluster assignments at the same time. Thus, we apply the actor-critic model (Konda and Tsitsiklis 2003) for optimization, which iteratively optimizes two groups of sub-networks.

Let ∇_ϕ , ∇_θ , ∇_ψ represent the gradients of the backpropagation process, respectively. We first fix the parameter of the prediction network (ϕ) to estimate parameters of feature extraction and subtype network (θ, ψ). By fixing ϕ , gradients ∇_θ can be given by:

$$\nabla_\theta = \frac{\partial L}{\partial \theta} = \sum_{m=1}^M \sum_{t=1}^{t_m} \left(\sum_{k=1}^K \|Y_m^t - \hat{Y}_m^t\|^2 \nabla_\theta E_m^t(k) - \lambda \nabla_\theta \sum_{k=1}^K E_m^t(k) \log(E_m^t(k)) \right)$$

Similarly, the gradients ∇_ψ can be given by:

$$\nabla_\psi = \frac{\partial L}{\partial \psi} = \sum_{m=1}^M \sum_{t=1}^{t_m} \left(\sum_{k=1}^K \|Y_m^t - \hat{Y}_m^t\|^2 \nabla_\psi E_m^t(k) - \lambda \nabla_\psi \sum_{k=1}^K E_m^t(k) \log(E_m^t(k)) \right)$$

At each stage, we update the subtype assignment by the updated subtype-specific features $\{C_m^t\}$. Then by fixing the feature extraction network and subtype network (θ, ψ), we iteratively update the prediction network whose gradient is given by:

$$\nabla_\phi = \frac{\partial L}{\partial \phi} = \sum_{m=1}^M \sum_{t=1}^{t_m} \frac{\partial l_m^t}{\partial \phi}$$

3 Results

3.1 Data Collection and Image Processing

The data used in this study was collected from Alzheimer's Disease Neuroimaging Initiative (ADNI) database. We retrieved (i) demographic

information, including age, gender, education, and occupation information; (ii) clinical assessment from a wide range of neuropsychological domains, including memory, executive, language, sociability, attention, etc.; (iii) longitudinal neuroimaging data, including Amyloid-, Tau-, and FDG-PET for AT[N] biomarker burden, and DWI for structural brain networks. Subjects selected here have two or more longitudinal scans and clinical assessment data.

Brain Network Construction. DWI images were aligned with each subject's T1-weighted MRI. We first parcellate brains to 148 regions based on the parcellation framework proposed in (Destrieux et al. 2010) and then applied the surface seed-based probabilistic fiber tractography in Free-Surfer (Reuter et al. 2012). The number of fibers connecting two brain regions is counted to measure the strength of the anatomical connectivity of pair-wise regions and stored in the connectivity matrix. A total of 506 structural brain networks were constructed from DWI images.

Regional AT[N] Level Acquisition. 2,807 amyloid PET (1,252 subjects), 1,009 tau PET (670 subjects), and 3,590 FDG PET (1,516 subjects) images were parcellated into 148 regions using Destrieux atlas (Destrieux et al. 2010) by aligning with each subject's T1-weighted MR image. We then calculate the regional standard uptake value ratio (SUVR) for amyloid-, tau-, and FDG-PET to represent the regional value of corresponding biomarkers, which is normalized by the whole cerebellum reference.

Cognitive Reserve. A computational proxy of the cognitive reserve (Y. Zhang et al. 2020) is used here to quantify the subject-specific network resilience to AT[N] pathology. Subjects' demographic data, socioeconomic factors, cerebrospinal fluid biomarkers, and AD-related polygenic risk are individually evaluated and serve as a moderator against neurodegeneration in our model.

Clinical Assessments. MMSE, ADAS, and CDR scores are indicators of subjects' overall cognition status and are used to guide our PSSN. We use Everyday Cognition Questionnaire (ECog) scores to validate and analyze our results. ECog is scored on a four-point scale where higher scores represent more severe dementia, based on one global factor and six domain-specific factors: everyday memory (ECogMem), language (ECogLang), visuospatial abilities (ECogVisspat), planning (ECogPlan), organization (ECogOrgan), and divided attention (ECogDivatt).

3.2 Experiment Setup and Parameter Tuning

To train our PSSN, the data (X and Y) is randomly split into training (80%) and validation (20%) sets. Since there is no ground truth for subtype assignments, we determine the optimal number of clusters by jointly considering cluster results from K-means, SuStain, and our PSSN. Taking K-means and SuStain as baselines, our method attains the lowest cluster variance ratio with respect to both K-means SuStain methods. Indeed, when $K = 6$, PSSN yields the lowest variance for all ECog scores except ECogOrgan ($K = 5$), as shown in Fig. 2.

We tested different hyperparameter combinations and chose $K = 6$, $\lambda = 10^{-5}$, $FC_dim = 8$, $keep_prob = 0.7$ as the final hyperparameters

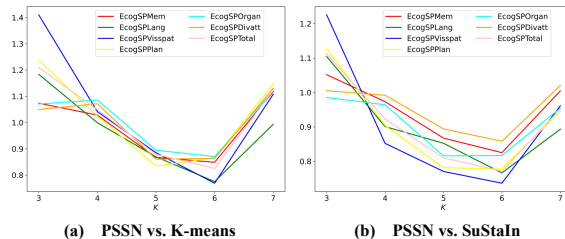


Fig. 2. Optimal number of subtypes. Intra-cluster variance ratios between (a) PSSN and K-means, (b) PSSN and SuStain with varying K , respectively.

of our stratification network, where K is the number of subtypes; λ is the parameter for calculating the loss function; FC_dim is the number of layers of the fully connected networks used in both the Subtype Network and the Prediction Network; $keep_prob$ is the probability of data kept at each dropout.

Table 1. Cluster sizes of K-means, SuStain, and PSSN methods.

	K-means	SuStain	PSSN
Subtype #1	275	207	211
Subtype #2	1115	238	217
Subtype #3	76	304	423
Subtype #4	237	861	743
Subtype #5	246	327	210
Subtype #6	10	22	155

3.3 Stratification Comparison

We use seven ECog scores (Mem, Lang, Visspat, Plan, Organ, Divatt, and Total) to evaluate the subtype stratification results as they reflect the clinical stages of AD progression and are unknown to all models.

We first analyze the distribution of subtype classification in three methods. As shown in Table 1, K-means and SuStain identified a giant cluster that includes more than 50% of observations despite extensive attempts. One possible explanation is their incapability of handling high-dimensional spatial data, where our input dimension is 148 brain regions. The elastic feature extraction network in PSSN can adapt to time series data with various lengths. Given the sporadic availability of neuroimaging data in real world, such a design maximizes the utility of available data.

Intra-cluster Homogeneity. We then investigate the consistency of clinical outcomes within each cluster. For each subtype identified by the PSSN, we calculate the variance of clinical scores to evaluate the quality of subtype classification, where a small variance indicates intra-cluster homogeneity. Fig. 3(a) shows the intra-cluster variance of seven ECogSP scores by K-means (top), SuStain (middle), and PSSN (bottom). Note that each column of the heatmap is individually normalized using column-wise z-scores, ensuring that each method is compared using the same mean and standard deviation values. Our PSSN method achieves superior intra-cluster consistency compared to K-means and SuStain in all ECog assessments.

Inter-cluster Heterogeneity. A pairwise t -test was performed to check the inter-cluster variance. In Fig. 3(b), we plot a triangle with $C_6^2 = 15$ grids where each grid represents the results of two-sample t -tests. As shown in Fig. 3(b), our PSSN method achieves the best performance since it has the least biased subtypes (pink grids, < 5% of subject pool) and the greatest number of pairs with significant inter-cluster differences (red grids, p -value < 0.05). We further rank each subtype according to the severity of averaged MMSE, CDR, and ADAS scores. It is found that our PSSN has the smallest cross-ranking links, indicating the best consistency within each subtype (Fig. 3(c)). With the lowest intra-cluster variance as well as the highest inter-cluster difference, our PSSN achieves the best coherence of all clinical assessments and sets a solid cornerstone for its clinical implications and applications.

3.4 Clinical Insights

Current diagnoses of AD are often delayed due to the wide spectrum of clinical symptoms among individuals. Given the fine-grained subtype

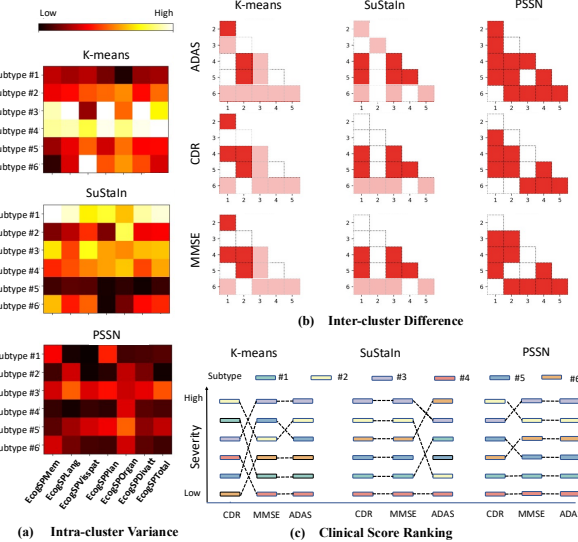


Fig. 3. Intra-cluster homogeneity and inter-cluster heterogeneity. (a) Intra-cluster Variance heatmap of ECog scores for PSSN, K-means and SuStain methods, where darker color represents lower variance. (b) Inter-cluster Variance: subtype pairs are marked red if the adjusted p -value across their MMSE, CDR and ADAS scores is significant (< 0.05). For significant subtype pairs, the grid is marked pink if at least one of these two subtypes is a biased subtype. (c) Trajectory plots of subtypes ranking according to MMSE, CDR and ADAS scores.

identified by our model, we further examine the distribution of ECog scores to explore the representative symptoms of each subtype.

ECog Entropy. To evaluate the inter-cluster difference of ECog scores, we calculate the cluster-wise entropy $E(L)$ in seven ECog scores:

$$E(L) = \left\{ - \sum_{i=1}^K p(l_{i,j}) \log_2 p(l_{i,j}) \mid j = 1, \dots, 7 \right\},$$

where j refers to the index of ECog scores, and $p(l_{i,j})$ is the probability of assigning the j^{th} ECog scores to i^{th} subtype. The average entropies of each ECog score are shown in Fig. 4(a). Compared to K-means and SuStain, our PSSN achieves the lowest entropies in all seven categories of ECog scores, showing the greatest stability in subtype identification.

Subtype Symptom. In Fig. 4(b), the six domains of ECog (except ECog-Totals) are mapped to six brain domains based on functional parcellation (see Fig. 4 for detailed brain region parcellation). Further in Fig. 4(c), we conclude the position of subtypes in the continuous spectrum: CN-like subtypes (#1, #4), MCI-like subtypes (#5, #6), and AD-like subtypes (#2, #3). The observed pattern summarized below offers new insight into the pre-diagnosis and treatment of AD as it inherently combines physiological and psychological markers.

AD State. As we can see clearly from Fig. 4(b), subtype #3 and subtype #2 present distinct cognitive levels in almost all domains. Subtype #3 has statistically significant higher scores than (i) subtype #4 in six domains (Organ, Divatt, Visspat, Mem, Lang, and Total), (ii) subtype #1 in domains (Plan, Divatt, Visspat, Mem, Lang, and Total). Subtype #2 is significantly higher than (i) subtypes #4 in Divatt, Mem, Lang, Total, (ii) subtype #1 in Divatt, Mem, Lang, Total, Plan, Visspat. This pattern also aligns with the predicted AT[N] level generated by our spatiotemporal model (discussed in Section 3.5). Based on the consistency of pathological biomarkers and clinical scores, we consider subtypes #3 and #2 as AD types, where high-level AT[N] accumulates across the brain and multiple symptoms manifest together simultaneously. Although it is hard to

Method/ EcogSP	Memory	Language	Visuospatial Abilities	Planning	Organization	Divided Attention	Total
MSSN	0.4798	0.4616	0.4390	0.4313	0.4474	0.4422	0.5424
K-means	0.6255	0.6676	0.6052	0.5680	0.6182	0.5850	0.7074
SuStain	0.8084	0.7590	0.6463	0.6479	0.6718	0.6396	0.9041

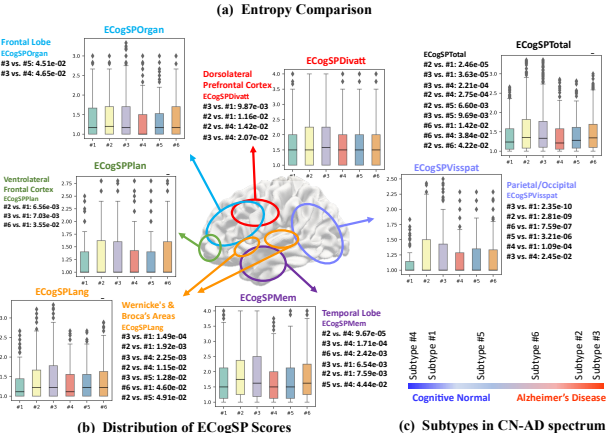


Fig. 4. Clinical interpretation of stratification results. (a) Entropy Comparison: ECog entropies across subtypes for K-means, SuStain, and PSSN methods. (b) Distribution of ECog scores. Each ECog score is mapped into a specific domain based on the functional parcellation of the human brain: temporal lobes regulate everyday memory (purple) (Squire and Zola-Morgan 1991), Wernicke's & Broca's areas regulate language (orange) (Blagoveshchenski et al. 2019), parietal and occipital lobes regulate visuospatial abilities (deep periwinkle) (Whittingstall et al. 2014), ventrolateral frontal cortex regulates planning (green) (Carrieri et al. 2018), frontal lobe regulates organization (blue) (Duncan et al. 1996), and dorsolateral prefrontal cortex regulates divided attention (red) (Johnson, Strafella, and Zatorre 2007). Each boxplot shows the distribution of corresponding clinical assessments. The pairwise t -test is used to measure the difference between subtypes, and all pairs with < 0.05 adjusted p -values are displayed next to the boxplot. Note the subtype with a higher mean ECog score is listed on the left-hand side. (c) Relative stages of six subtypes on AD spectrum based on ECog scores.

differentiate subtypes #3 and #2 based on reported symptoms, we could observe distinct patterns of pathological burdens Fig. 5(a).

CN State. Subtypes #1 and #4 are on the other end of the AD spectrum as they have the lowest grades in almost all domains. A closer look at the clinical scores reveals that subtype #1 has particularly low scores on planning and visuospatial abilities, implying low AT[N] accumulations in the ventrolateral frontal cortex, parietal lobe, and occipital lobe, which is further validated by the subtypes' phenotypes shown in Fig. 5(a). Subtype #4 scores are significantly lower in memory, which is also consistent with the brain mapping of AT[N] biomarkers. A further examination shows that subtype #4 has more problems with visual-spatial abilities, which suggests subtype-specific treatments in parietal and occipital lobes and could be used in clinical settings to differentiate subtypes #4 and #1.

MCI State. Subtypes #5 and #6 are intermediate states. Subtype #5 scores significantly higher on memory than subtype #4 and on visual-spatial ability than subtype #1. Subtype #6 has higher scores in almost all cognitive domains than subtypes #1, #4, which implies subtype #6 should be placed closer to the AD end on cognitive continuums. Subtype #5 has close to normal organization and language abilities, while subjects in subtype #6 tend to score higher in planning, language abilities, and total assessments. Such distinction suggests heavier pathologic burdens in Subtype #6's Wernicke's and Broca's areas, which is confirmed in Fig. 5(a).

3.5 Neurobiological Evaluation

Due to the massive heterogeneity between neurobiological examination and clinical diagnosis, we are interested in the associated neurobiological factors for each identified subtype. We compute the subtype transition matrix, analyze the corresponding AT[N] pattern, and generalize an AD evolutionary graph for subtype prognosis.

Transition Matrix. As defined above, each subject is labeled as s_m^t which is the subtype index (from 1 to $K = 6$) of subject m at visit t . Since subjects may transit from one subtype to another, we record the occurrence of such transitions by ordered pairs defined as $Q = \{q_i | i = 1, \dots, K\} = \{(s_m^t, s_m^{t+1}) | m = 1, \dots, M, t = 1, \dots, t_m - 1\}$. Each q_i represents all the transition pairs starting in subtype $\#i$. We then count the frequency of ordered pairs and calculate the row stochastic transition matrix $Pr = [pr_{i,j}]$, $i, j = 1, \dots, K$, where

$$pr_{i,j} = \frac{|\{(s_m^t, s_m^{t+1}) | s_m^t = i, s_m^{t+1} = j\}|}{|q_i|}$$

is the possibility of subtype $\#i$ transiting to subtype $\#j$.

AT[N] Pattern. We check the topological patterns of average AT[N] burden across brain networks to investigate the relationship with their clinical outcomes, indicated by AT[N] pattern (Fig. 5(a)) and subtype-typical clinical profiles (Fig. 4(b)). Consistent with normal cognitive functions reflected by ECog scores, AT[N] burdens are the lowest for subtype #4 except for parietal and occipital lobes, which matches the jump of visuospatial scores. For subtype #1, only mild AT[N] burden is observed across the brain. Despite relatively higher tau levels in the superior and inferior temporal gyrus, the neuron loss is not noticeable in the temporal lobe, which could explain subtype #1's significantly better memory abilities. Close attention should be paid to this cohort if they experience a sudden decline in memory. Subtype #5 resides in the intermediate state of AD spectrum. Subtype #6 is also in the intermediate state but closer to AD state with elevated tau and neurodegeneration level in temporal lobes, which accords with ECog memory score. Subtypes #2 and #3 are identified as AD state since they have significantly higher whole-brain AT[N] levels and clinical scores in all domains. Subtype #3 tends to harbor more neurodegeneration in Wernicke's area than subtype #2, including angular gyrus and supramarginal gyrus that are in the parietal lobe (Stippich et al. 2007). Thus, subtype #3 is more susceptible to declined comprehension ability, leading to severe survival problems in real-life situations (Robson et al. 2014).

In Fig. 5(a), we connect each subtype-wise average AT[N] pattern using the obtained transition matrix, where thicker arrows represent high transition probability. Subtype #4 has the lowest AT[N] level in the prefrontal cortex and has a 23.5% probability of converting to subtype #1, which accumulates more pathological burdens in the prefrontal cortex. Subtype #1 has a 16% probability of converting to the intermediate state, subtype #5, and then to subtype #6. These MCI states each have around 40% probability of developing into AD state, which is marked by further increments of AT[N] accumulations across the exocortex. Fig. 5(b) summarizes hypothetical CN, MCI, AD pathways, which are congruent with the order of subtypes on the continuum in Fig. 4(c), demonstrating the consistency between physiological and psychological signs using our pathology steered method. Clinicians should closely monitor their cognitive abilities and provide prompt intervention if there is a sudden deterioration.

Final Stable State. For the subtype transition matrix Pr , each subtype can be considered as a node in a graph, and the transition probability indicates the directed link between two subtypes. As the initial distribution of subtypes in our subject pool is $\pi^{(0)} = \{0.11, 0.11, 0.22, 0.38, 0.11, 0.08\}$ and $\pi^{(n)} = \pi^{(0)}Pr^n$, we can get the steady state vector v of the transition matrix by taking the infinite limit of n , written as $v = \pi^{(0)} \cdot \lim_{n \rightarrow \infty} Pr^n$. Fig. 6 shows the transition matrix at different steps

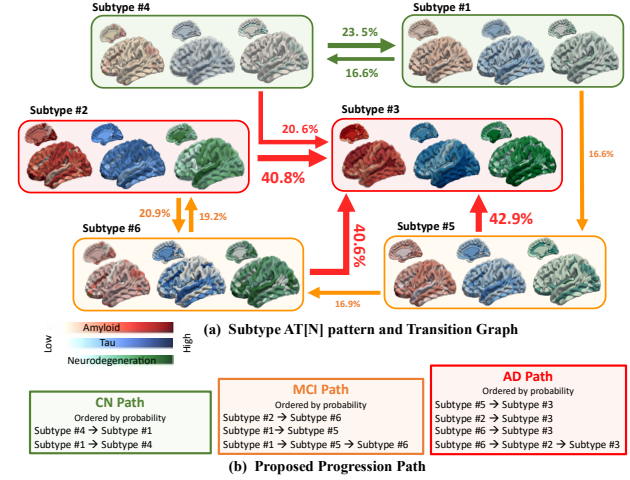


Fig. 5. Hypothetical subtype transition graph in AD progression. (a) The subtype conversion diagram was drawn upon the count of subjects converting from one subtype to another. The probability of transition is labeled next to each arrow and indicated by the arrow width. The inside rounded box shows the AT[N] burden of each subtype, where the lightness of color represents the level of AT[N] biomarker (red for A, blue for T, green for [N]). Only transitions with probabilities $> 16\%$ were plotted in the diagram. (b) Subtype brains with low, intermediate, and high AT[N] values are mapped to CN-, MCI-, and AD-like states. We summarize possible CN/MCI/AD pathways based on starting and ending states.

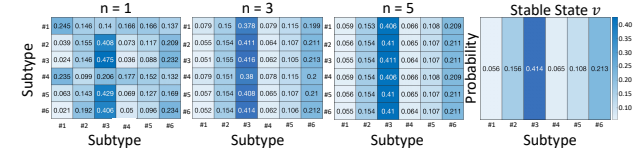


Fig. 6. Heatmaps of subtype transition matrix at different time steps (n). The number and shade in entry i^{th} row and j^{th} column represent the probability of transitioning from subtype $\#i$ to subtype $\#j$ at a given time.

($n = 1, 3, 5$) using heatmaps, where darker colors represent higher transition probabilities. When $n = 0$, the heatmap is the initial transition matrix. As we increase the exponent, the matrix approaches the stable state vector v . We can calculate v by solving $Pr \cdot v = v$, which is the eigenvector of the transition matrix corresponding to the eigenvalue $\lambda = 1$. More than 50% of subjects will progress to AD states (subtypes #2 and #3), 33% of subjects will stay in MCI state (subtypes #5 and #6), and only 13% of subjects will stay in cognitive normal states (subtypes #1 and #4).

4 Conclusions

In this paper, we propose a pathology steered stratification network to fill the domain knowledge gap in current study of AD subtype identification. Our proposed method integrates (1) a state-of-art reaction-diffusion model that can identify causality and mechanisms underlying Alzheimer's and characterize the spatiotemporal dynamics of AT[N] biomarkers across brain networks; (2) a deep predictive neural network that can learn representative features of neurodegeneration trajectories and stratify the aging population into fine-grained subtypes with distinct pathological profiles. Compared to other methods like K-means and SuStAlN, our PSSN achieves the highest inter-cluster heterogeneity and intra-cluster homogeneity. Importantly, we discovered six distinct subtypes spread across neurodegeneration spectrum, where each subtype shows consistency between neurobiological burden and symptom profiles, indicating the potential of our PSSN to disentangle AD heterogeneity. A disease evolutionary graph

is presented as a general guideline for probable state transition of subtypes. Altogether, our method provides a systematic way of subtype identification with joint consideration of existing pathological knowledge, physiological imaging data, and psychological examinations, which can assist pre-clinical AD prognosis and may be applied to other neurodegenerative studies facing similar therapeutic challenges.

Acknowledgments

The work is supported by NIH R03AG073927 and Wake Forest University Pilot Grant Funding.

References

Aisen, Paul S., Ronald C. Petersen, Michael C. Donohue, Anthony Gamst, Rema Raman, Ronald G. Thomas, Sarah Walter, et al. 2010. "Clinical Core of the Alzheimer's Disease Neuroimaging Initiative: Progress and Plans." *Alzheimer's & Dementia* 6 (3): 239–46. <https://doi.org/10.1016/j.jalz.2010.03.006>.

Aksman, Leon M., Peter A. Wijeratne, Neil P. Oxtoby, Arman Eshaghi, Cameron Shand, Andre Altmann, Daniel C. Alexander, and Alexandra L. Young. 2021. "PySuStAIn: A Python Implementation of the Subtype and Stage Inference Algorithm." *SoftwareX* 16 (December): 100811. <https://doi.org/10.1016/j.softx.2021.100811>.

Ballatore, Carlo, Virginia M.-Y. Lee, and John Q. Trojanowski. 2007. "Tau-Mediated Neurodegeneration in Alzheimer's Disease and Related Disorders." *Nature Reviews. Neuroscience* 8 (9): 663–72. <https://doi.org/10.1038/nrn2194>.

Bertsch, Michiel, Bruno Franchi, Norina Marcello, Maria Carla Tesi, and Andrea Tosini. 2017. "Alzheimer's Disease: A Mathematical Model for Onset and Progression." *Mathematical Medicine and Biology: A Journal of the IMA* 34 (2): 193–214. <https://doi.org/10.1093/imammb/dqw003>.

Bertsch, Michiel, Bruno Franchi, Ashish Raj, and Maria Carla Tesi. 2021. "Macroscopic Modelling of Alzheimer's Disease: Difficulties and Challenges." *Brain Multiphysics* 2 (January): 100040. <https://doi.org/10.1016/j.brain.2021.100040>.

Blagovechtchenski, Evgeny, Daria Gnedykh, Diana Kurmakaeva, Nadezhda Mkrtchyan, Svetlana Kostromina, and Yury Shtyrov. 2019. "Transcranial Direct Current Stimulation (TDCS) of Wernicke's and Broca's Areas in Studies of Language Learning and Word Acquisition." *Journal of Visualized Experiments: JoVE*, no. 149 (July). <https://doi.org/10.3791/59159>.

Bloom, George S. 2014. "Amyloid- β and Tau: The Trigger and Bullet in Alzheimer Disease Pathogenesis." *JAMA Neurology* 71 (4): 505–8. <https://doi.org/10.1001/jamaneurol.2013.5847>.

Braak, H., and E. Braak. 1991. "Neuropathological Stageing of Alzheimer-Related Changes." *Acta Neuropathologica* 82 (4): 239–59. <https://doi.org/10.1007/BF00308809>.

———. 1996. "Evolution of the Neuropathology of Alzheimer's Disease." *Acta Neuropathologica Scandinavica* 94 (S165): 3–12. <https://doi.org/10.1111/j.1600-0404.1996.tb05866.x>.

Busche, Marc Aurel, and Bradley T. Hyman. 2020. "Synergy between Amyloid- β and Tau in Alzheimer's Disease." *Nature Neuroscience* 23 (10): 1183–93. <https://doi.org/10.1038/s41593-020-0687-6>.

Carrieri, Marika, Stefania Lancia, Alessia Bocchi, Marco Ferrari, Laura Piccardi, and Valentina Quaresima. 2018. "Does Ventrolateral Prefrontal Cortex Help in Searching for the Lost Key? Evidence from an fNIRS Study." *Brain Imaging and Behavior* 12 (3): 785–97. <https://doi.org/10.1007/s11682-017-9734-7>.

Cope, Thomas E., Timothy Rittman, Robin J Borchert, P Simon Jones, Deniz Vatansever, Kieren Allinson, Luca Passamonti, et al. 2018. "Tau Burden and the Functional Connectome in Alzheimer's Disease and Progressive Supranuclear Palsy." *Brain* 141 (2): 550–67. <https://doi.org/10.1093/brain/awx347>.

Destrieux, Christophe, Bruce Fischl, Anders Dale, and Eric Halgren. 2010. "Automatic Parcellation of Human Cortical Gyri and Sulci Using Standard Anatomical Nomenclature." *NeuroImage* 53 (1): 1–15. <https://doi.org/10.1016/j.neuroimage.2010.06.010>.

Dickerson, Bradford C., Reisa A. Sperling, Bradley T. Hyman, Marilyn S. Albert, and Deborah Blacker. 2007. "Clinical Prediction of Alzheimer Disease Dementia Across the Spectrum of Mild Cognitive Impairment." *Archives of General Psychiatry* 64 (12): 1443–50. <https://doi.org/10.1001/archpsyc.64.12.1443>.

Ding, Yiming, Jae Ho Sohn, Michael G. Kawczynski, Hari Trivedi, Roy Harnish, Nathaniel Dmytro Litiev, et al. 2019. "A Deep Learning Model to Predict a Diagnosis of Alzheimer Disease by Using 18F-FDG PET of the Brain." *Radiology* 290 (2): 456–64. <https://doi.org/10.1148/radiol.2018180958>.

Duncan, J., H. Emslie, P. Williams, R. Johnson, and C. Freer. 1996. "Intelligence and the Frontal Lobe: The Organization of Goal-Directed Behavior." *Cognitive Psychology* 30 (3): 257–303. <https://doi.org/10.1006/cogp.1996.0008>.

Frost, Georgia R., and Yue-Ming Li. 2017. "The Role of Astrocytes in Amyloid Production and Alzheimer's Disease." *Open Biology* 7 (12): 170228. <https://doi.org/10.1098/rsob.170228>.

Habes, Mohamad, Michel J. Grothe, Birkan Tunc, Corey McMillan, David A. Wolk, and Christos Davatzikos. 2020. "Disentangling Heterogeneity in Alzheimer's Disease and Related Dementias Using Data-Driven Methods." *Biological Psychiatry, Convergence and Heterogeneity in Psychopathology*, 88 (1): 70–82. <https://doi.org/10.1016/j.biopsych.2020.01.016>.

Hao, Wenrui, and Avner Friedman. 2016. "Mathematical Model on Alzheimer's Disease." *BMC Systems Biology* 10 (1): 108. <https://doi.org/10.1186/s12918-016-0348-2>.

Holtzman, David M., John C. Morris, and Alison M. Goate. 2011. "Alzheimer's Disease: The Challenge of the Second Century." *Science Translational Medicine*, April. <https://doi.org/10.1126/scitranslmed.3002369>.

Ikonomovic, Milos D., Chris J. Buckley, Kerstin Heurling, Paul Sherwin, Paul A. Jones, Michelle Zanette, Chester A. Mathis, et al. 2016. "Post-Mortem Histopathology Underlying β -Amyloid PET Imaging Following Flutemetamol F 18 Injection." *Acta Neuropathologica Communications* 4 (1): 130. <https://doi.org/10.1186/s40478-016-0399-z>.

Jack, Clifford R., David A. Bennett, Kaj Blennow, Maria C. Carrillo, Billy Dunn, Samantha Budd Haeberlein, David M. Holtzman, et al. 2018. "NIA-AA Research Framework: Toward a Biological Definition of Alzheimer's Disease." *Alzheimer's & Dementia: The Journal of the Alzheimer's Association* 14 (4): 535–62. <https://doi.org/10.1016/j.jalz.2018.02.018>.

Jack, Clifford R., and David M. Holtzman. 2013. "Biomarker Modeling of Alzheimer's Disease." *Neuron* 80 (6): 1347–58. <https://doi.org/10.1016/j.neuron.2013.12.003>.

Jack, Clifford R., Jr, Val J. Lowe, Stephen D. Weigand, Heather J. Wiste, Matthew L. Senjem, David S. Knopman, Maria M. Shiung, et al. 2009. "Serial PIB and MRI in Normal, Mild Cognitive Impairment and Alzheimer's Disease: Implications for Sequence of Pathological Events in Alzheimer's Disease." *Brain* 132 (5): 1355–65. <https://doi.org/10.1093/brain/awp062>.

Jack, C.R., M.M. Shiung, J.L. Gunter, P.C. O'Brien, S.D. Weigand, D.S. Knopman, B.F. Boeve, et al. 2004. "Comparison of Different MRI Brain Atrophy Rate Measures with Clinical Disease Progression in AD." *Neurology* 62 (4): 591–600.

Johnson, David K., Martha Storandt, John C. Morris, and James E. Galvin. 2009. "Longitudinal Study of the Transition From Healthy Aging to Alzheimer Disease." *Archives of Neurology* 66 (10): 1254–59. <https://doi.org/10.1001/archneurol.2009.158>.

Johnson, Jennifer Adrienne, Antonio P. Strafella, and Robert J. Zatorre. 2007. "The Role of the Dorsolateral Prefrontal Cortex in Bimodal Divided Attention: Two Transcranial Magnetic Stimulation Studies." *Journal of Cognitive Neuroscience* 19 (6): 907–20. <https://doi.org/10.1162/jocn.2007.19.6.907>.

Konda, Vijay R., and John N. Tsitsiklis. 2003. "OnActor-Critic Algorithms." *SIAM Journal on Control and Optimization* 42 (4): 1143–66. <https://doi.org/10.1137/S0363012901385691>.

Lam, Benjamin, Mario Masellis, Morris Freedman, Donald T. Stuss, and Sandra E. Black. 2013. "Clinical, Imaging, and Pathological Heterogeneity of the Alzheimer's Disease Syndrome." *Alzheimer's Research & Therapy* 5 (1): 1. <https://doi.org/10.1186/alzrt155>.

Li, Wenchao, Defu Yang, Chenggang Yan, Minghan Chen, Quefeng Li, Wentao Zhu, Guorong Wu, and Alzheimer's Disease Neuroimaging Initiative. 2022. "Characterizing Network Selectiveness to the Dynamic Spreading of Neuropathological Events in Alzheimer's Disease." *Journal of Alzheimer's Disease: JAD* 86 (4): 1805–16. <https://doi.org/10.3233/JAD-215596>.

Li, Wenchao, Jiaqi Zhao, Chenyu Shen, Jingwen Zhang, Ji Hu, Mang Xiao, Jiyong Zhang, and Minghan Chen. 2022. "Regional Brain Fusion: Graph Convolutional Network for Alzheimer's Disease Prediction and Analysis." *Frontiers in Neuroinformatics* 16. <https://www.frontiersin.org/articles/10.3389/fninf.2022.886365>.

Petrella, Jeffrey R., Wenrui Hao, Adithi Rao, and P. Murali Doraiswamy. 2019. "Computational Causal Modeling of the Dynamic Biomarker Cascade in Alzheimer's Disease." *Computational and Mathematical Methods in Medicine* 2019 (February): e6216530. <https://doi.org/10.1155/2019/6216530>.

Raj, Ashish. 2021. "Graph Models of Pathology Spread in Alzheimer's Disease: An Alternative to Conventional Graph Theoretic Analysis." *Brain Connectivity* 11 (10): 799–814. <https://doi.org/10.1089/brain.2020.0905>.

Raj, Ashish, Amy Kuceyeski, and Michael Weiner. 2012. "A Network Diffusion Model of Disease Progression in Dementia." *Neuron* 73 (6): 1204–15. <https://doi.org/10.1016/j.neuron.2011.12.040>.

Raj, Ashish, Eve LoCastro, Amy Kuceyeski, Duygu Tosun, Norman Relkin, and Michael Weiner. 2015. "Network Diffusion Model of Progression Predicts Longitudinal Patterns of Atrophy and Metabolism in Alzheimer's Disease." *Cell Reports* 10 (3): 359–69. <https://doi.org/10.1016/j.celrep.2014.12.034>.

Reuter, Martin, Nicholas J. Schmansky, H. Diana Rosas, and Bruce Fischl. 2012. "Within-Subject Template Estimation for Unbiased Longitudinal Image Analysis." *Neuroimage* 61 (4): 1402–18. <https://doi.org/10.1016/j.neuroimage.2012.02.084>.

Robson, Holly, Roland Zahn, James L. Keidel, Richard J. Binney, Karen Sage, and Matthew A. Lambon Ralph. 2014. "The Anterior Temporal Lobes Support Residual Comprehension in Wernicke's Aphasia." *Brain: A Journal of Neurology* 137 (Pt 3): 931–43. <https://doi.org/10.1093/brain/awt373>.

Squire, L. R., and S. Zola-Morgan. 1991. "The Medial Temporal Lobe Memory System." *Science (New York, N.Y.)* 253 (5026): 1380–86. <https://doi.org/10.1126/science.1896849>.

Stippich, Christoph, Nora Rapps, Jens Dreyhaupt, Anita Durst, Bodo Kress, Ernst Nennig, Volker M. Tronnier, and Klaus Sartor. 2007. "Localizing and Lateralizing Language in Patients with Brain Tumors: Feasibility of Routine Preoperative Functional MR Imaging in 81 Consecutive Patients." *Radiology* 243 (3): 828–36. <https://doi.org/10.1148/radiol.243060068>.

Venugopalan, Janani, Li Tong, Hamid Reza Hassanzadeh, and May D. Wang. 2021. "Multimodal Deep Learning Models for Early Detection of Alzheimer's Disease Stage." *Scientific Reports* 11 (1): 3254. <https://doi.org/10.1038/s41598-020-74399-w>.

Vogel, Jacob W., Alexandra L. Young, Neil P. Oxtoby, Ruben Smith, Rik Ossenkoppele, Olof T. Strandberg, Renaud La Joie, et al. 2021. "Four Distinct Trajectories of Tau Deposition Identified in Alzheimer's Disease." *Nature Medicine* 27 (5): 871–81. <https://doi.org/10.1038/s41591-021-01309-6>.

Whittingstall, Kevin, Michael Bernier, Jean-Christophe Houde, David Fortin, and Maxime Descoteaux. 2014. "Structural Network Underlying Visuospatial Imagery in Humans." *Cortex: a Journal Devoted to the Study of the Nervous System and Behavior* 56 (July): 85–98. <https://doi.org/10.1016/j.cortex.2013.02.004>.

Yang, Zhijian, Ilya M. Nasrallah, Haochang Shou, Junhao Wen, Jimit Doshi, Mohamad Habes, Guray Erus, et al. 2021. "A Deep Learning Framework Identifies Dimensional Representations of Alzheimer's Disease from Brain Structure." *Nature Communications* 12 (1): 7065. <https://doi.org/10.1038/s41467-021-26703-z>.

Young, Alexandra L., Razvan V. Marinescu, Neil P. Oxtoby, Martina Bocchetta, Keir Yong, Nicholas C. Firth, David M. Cash, et al. 2018. "Uncovering the Heterogeneity and Temporal Complexity of Neurodegenerative Diseases with Subtype and Stage Inference." *Nature Communications* 9 (1): 4273. <https://doi.org/10.1038/s41467-018-05892-0>.

Zhang, Jingwen, Defu Yang, Wei He, Guorong Wu, and Minghan Chen. 2020. "A Network-Guided Reaction-Diffusion Model of AT[N] Biomarkers in Alzheimer's Disease." In *2020 IEEE 20th International Conference on Bioinformatics and Bioengineering (BIBE)*, 222–29. <https://doi.org/10.1109/BIBE50027.2020.00044>.

Zhang, Ying, Yajing Hao, Lang Li, Kai Xia, Guorong Wu, and Alzheimer's Disease Neuroimaging Initiative. 2020. "A Novel Computational Proxy for Characterizing Cognitive Reserve in Alzheimer's Disease." *Journal of Alzheimer's Disease: JAD* 78 (3): 1217–28. <https://doi.org/10.3233/JAD-201011>.